minerals

MDPI

Article

Influence of Chromite Ore Selection on the Pelletized Oxidative Sintering Process: A South African Case Study

Yolindi van Staden [1], Stephanus Petrus du Preez [2,*], Johan Paul Beukes [1,*], Pieter Gideon van Zyl [1] and Jason Groenewald [1]

[1] Chemical Resource Beneficiation, North-West University, Potchefstroom 2531, South Africa; yolindivanstaden@outlook.com (Y.v.S.); pieter.vanzyl@nwu.ac.za (P.G.v.Z.); groenewald.jason@gmail.com (J.G.)
[2] Hydrogen South Africa (HySA) Infrastructure, Faculty of Engineering, North-West University, Potchefstroom 2531, South Africa
* Correspondence: faan.dupreez@nwu.ac.za (S.P.d.P.); paul.beukes@steinert.com.au (J.P.B.)

Abstract: The smelting of chromite to produce ferrochrome (FeCr) and subsequently, stainless steel, is an energy-intensive carbothermic process. Various countries apply the Outotec FeCr process, which employs oxidative sintering in air to produce mechanically strong chromite pellets. During this process, iron (Fe) is liberated from the chromite spinel due to the elevated temperatures and oxidative nature of the process. It is well understood that oxidatively altered chromite requires less energy to be smelted when compared to non-oxidized chromite. This study showed that sintered pellets obtained from five South African pellet sintering plants had vastly different oxidative alteration penetrations. Additionally, sintered pellets from the same plant may also vary significantly. It was further shown that ores mined from various locations in South Africa had dissimilar sintering behaviors, suggesting that sintered pellets should be characterized before smelting to determine the extent of oxidative alteration. The benefit of a smelter consuming oxidized ore was also demonstrated by comparing the interaction between oxidized and non-oxidized chromite with a carbon (C) source.

Keywords: pelletized oxidative sintering; Outotec ferrochrome process; chromite; thermal gravimetric analysis (TGA); oxidative alteration

Citation: van Staden, Y.; du Preez, S.P.; Beukes, J.P.; van Zyl, P.G.; Groenewald, J. Influence of Chromite Ore Selection on the Pelletized Oxidative Sintering Process: A South African Case Study. *Minerals* **2024**, *14*, 1203. https://doi.org/10.3390/min14121203

Academic Editor: Rajesh Kumar Jyothi

Received: 8 October 2024
Revised: 11 November 2024
Accepted: 21 November 2024
Published: 26 November 2024

1. Introduction

Stainless steel is a vital modern-day alloy, with many applications. The chromium (Cr) content in stainless steel is principally what makes it "stainless". The Cr units in stainless steel are obtained from stainless-steel scrap recycling and ferrochrome (FeCr), a relatively crude alloy that primarily contains Cr and iron (Fe). Four FeCr grades are produced commercially, i.e., high-carbon (C) FeCr (typically > 60% Cr and 6%–9% C), charge-grade FeCr (typically 50%–60% Cr and 6%–9% C), medium C FeCr (typically 56%–70% Cr and 1%–4% C), and low C FeCr (typically 56%–70% Cr and 0.015%–1.0% C) [1–3]. Since the development of the argon oxygen decarburization (AOD) and vacuum oxygen decarburization (VOD) processes, which allow for the removal of C from stainless-steel melts with acceptable losses of Cr, the demand for low- and medium-grade C FeCr has decreased dramatically. For instance, in 2019, medium and low C FeCr accounted for less than 6.9% of the global annual FeCr production [4–6]. High C FeCr and charge-grade FeCr are somewhat similar in composition, therefore these two grades are commonly combined and referred to as high C charge-grade FeCr [4].

Four relatively well-defined process combinations are used by most high C charge-grade FeCr producers [7,8], i.e., (i) conventional open/semi-closed submerged arc furnace (SAF) operation consuming coarse (typically 6–150 mm) chromite ore and/or agglomerated chromite in the presence of coarse carbonaceous reductants and coarse fluxes; (ii) closed SAF operation consuming oxidative sintered pelletized chromite feed together with coarse

reductants and fluxes, which is commercially known as the "Outotec FeCr process" [8–11]; (iii) closed SAF operation consuming pre-reduced chromite pelletized feed, together with coarse reductants and fluxes, which is commercially known as the Premus Process [12–15]; and (iv) direct current (DC) arc furnace operation, which can exclusively consume fine chromite, carbonaceous, and fluxes [16,17].

South Africa has a significant number of FeCr production sites, which leverages a range of furnace technologies. Considering the general frail nature of chromite ore [18], a pelletization step is required prior to smelting [19]. Considering the relatively low capital and running costs associated with the Outotec process when compared to Premus operations, the Outotec process is preferred. Therefore, the Outotec process is of particular importance within the South African landscape. Most of the chromite mined in South Africa is sourced from a large, layered intrusion known as the Bushveld Complex, which holds the largest chromite deposits in the world [20–22]. The area is divided into three zones, i.e., the Upper and Lower Zone, the Upper and Lower Critical Zone, and the Main Zone. Chromite is mainly found within the Critical Zone. It has been proposed that exploitable chromite is mostly found in 13 chromitite layers in the Lower Critical Zone [23,24]. The chromitite layers form continuous layers that are classified into three groups, i.e., the Lower Group (LG), the Middle Group (MG), and the Upper Group (UG) [25]. The LG group is further divided into LG1 to LG7, the MG group into MG0 to MG4, and the UG group into UG1 to UG3 [25,26]. The chromitite layers in the Bushveld Complex exhibit thicknesses ranging from just a few cm to up to 2–3 m. Due to extensive mining, these chromitite layers can be traced across nearly the entire 400 km breadth of the Bushveld Complex, indicating a widespread, continuous formation process. Studies have suggested that this formation was likely synchronized over large lateral distances, resulting in highly uniform layers of chromitites. Such findings underscore the geological stability and continuity in chromitite layer deposition within the complex, supporting hypotheses that formation mechanisms operated simultaneously across the region [22,25,27–29].

The chemistry and geological setting of the different groups within the Bushveld Complex have been the focus of various studies [20,30,31]. The characteristics, such as chemical and mineral compositions and Cr/Fe ratios, of chromite mined from the different groups can vary significantly [20,24,30,31]. These differences make the Bushveld Complex the ideal place to gather case study ores that are used for smelting.

The current work considers aspects of the pelletized oxidative sintering process, i.e., the Outotec process. This technology has been commonly applied in many countries, in both green and brownfield expansions. The pelletized oxidative sintering process involves several steps [8,32,33]. Firstly, fine chromite ore (typically < 1 mm) is wet milled, together with a small percentage (1–2 wt%) of fine carbonaceous material (e.g., coke, anthracite, or char) to prepare a homogenous mixture with a particle size distribution in which 80% of the particle are below 74 µm. Hereafter, the mixture is dewatered using ceramic filters to typically 8.5–9 wt% moisture. Approximately 1 wt% refined clay, which serves as a binder, is then mixed into the moist milled mixture. This mixture is then pelletized in a pelletizing drum, where the over- and undersized green pellets are recycled. Appropriately sized green pellets, between 9 and 13 mm, are then layered on a perforated stainless-steel sintering belt, which is protected against excessive temperatures during the sintering process by a layer of pellets that were already sintered. The pellets are then carried through a multicompartment furnace wherein the green pellet C is consumed as an oxidative energy source [8,33].

Several metallurgical advantages exist for downstream smelters consuming pelletized oxidatively sintered chromite [8,34]. Of specific interest here is the possible liberation of Fe from the chromite spinel. Several authors have shown that Fe can be liberated from the chromite spinel during the pelletized oxidative sintering process (e.g., [32,35,36]). Additionally, several studies have shown that sintered (or pre-oxidized) chromite reduces at a lower temperature when compared to raw chromite (e.g., [37–39]). Chromite ore reduced with hydrogen also proceeded to a greater degree if pre-oxidized [40]. The liberated Fe forms a Fe_2O_3 sesquioxide phase that is observed in a typical Widmanstätten

pattern [37,41–44]. To visualize the formation of the sesquioxide phase, an example thereof is taken from a non-related study by Du Preez et al. (2019) and is presented in Figure 1 [36].

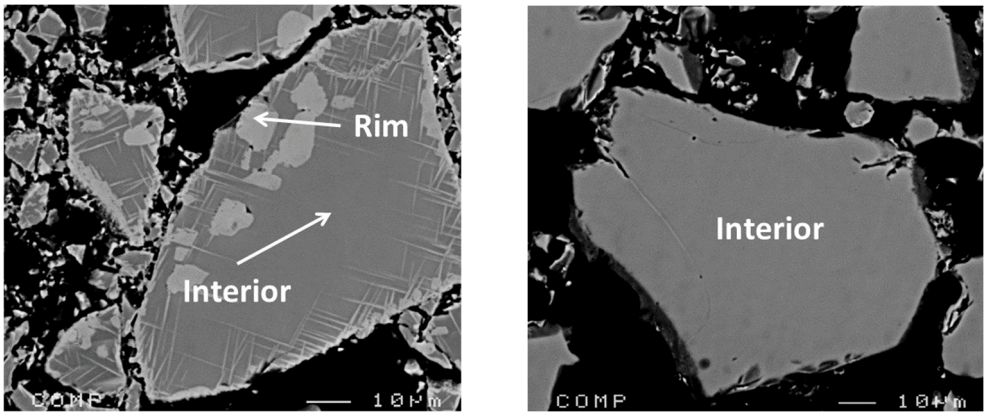

(**a**) (**b**)

Figure 1. Backscatter electron SEM micrograph of chromite grains near the edge of a cross-sectioned polished oxidative sintered pellet (**a**); a corresponding micrograph of grains toward the center of the pellet (**b**) [36] (reused under license Creative Commons Attribution (CC BY)).

Figure 1a shows the formed Fe_2O_3-enriched sesquioxide phase (shown as the light grey areas within the grain) visible in chromite grains near the edge of an oxidative sintered pellet, while the sesquioxide phase formation did not occur in chromite grains near the center of the same pellet [36]. The formation of the sesquioxide phase is due to chromite's decomposition, which follows the generalized spinel phase decomposition as shown in Equation (1) [36,45,46].

$$(A)[B]_2O_4 = (AO) + [B_2O_3] \quad (1)$$

Here, A and B are taken as Fe and Cr, respectively. The FeO phase, which has been liberated from the chromite spinel, is of importance. Considering the partial oxidative atmosphere during sintering, the liberated FeO is further subjected to oxidation, i.e., Fe^{2+} as FeO to Fe^{3+} as Fe_2O_3 [40,46]. To illustrate the difference in reducibility of the various metal oxides by C, an Ellingham diagram is presented in Figure 2 [38]. Figure 2 shows that for Fe_2O_3, the interaction with C proceeds at approximately 320 °C and is reduced to the intermediate Fe-oxide, Fe_3O_4. Hereafter, Fe_3O_4 reduces to FeO at approximately 685 °C and FeO to metallic Fe^0 at approximately 720 °C (indicated with the solid red line). In contrast, pure chromite (represented as Cr_2FeO_4) is expected to be metalized to Fe^0 and Cr^0 by C at approximately 1250 °C (indicated with the dashed red line). Therefore, increased Fe liberation and the associated Fe-oxide formation will significantly reduce the specific energy consumption (SEC) (i.e., the energy required per ton of FeCr produced) of a particular SAF that is fed with oxidative sintered pellets.

Considering the above-mentioned benefit associated with increased Fe liberation from the spinel, it is vital to optimize liberation during the pelletized oxidative sintering process. This work was partially motivated by the observation of operational personnel that sintering plants found it difficult to sustain oxidative sintered pellet characteristics over prolonged periods, notwithstanding that key operational parameters, e.g., particle size distribution, green pellet C and binder contents, pellet diameter range, and temperatures in the multi-compartment sintering furnace, were maintained relatively stable. In the current work, the extent of chromite oxidative alteration of industrially produced oxidative sintered pellets from five different sintering plants was characterized. In addition, the amenabilities to oxidative alteration of six dissimilar chromite ores were investigated to demonstrate the effect the selected ore could have on the sintering process.

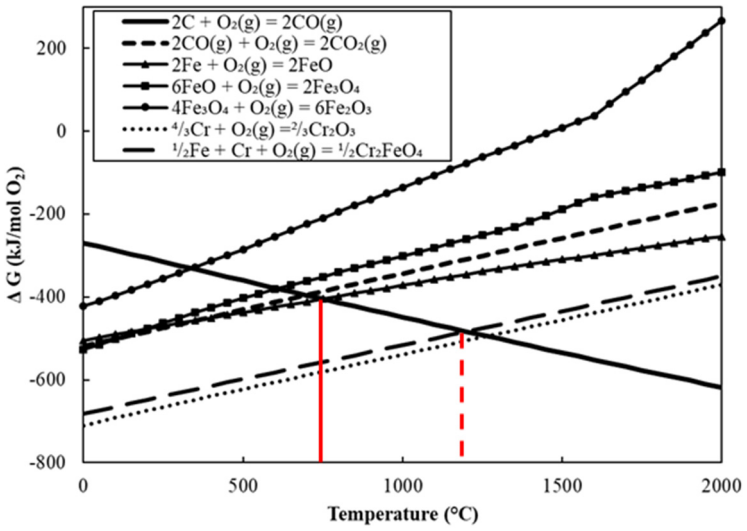

Figure 2. Ellingham diagram (Gibbs free energy, ΔG) indicating the reduction of metal oxides with solid C and CO, constructed with HSC thermo-chemical software 10 [38] (reused with permission from Kleynhans et al., Minerals Engineering, published by Elsevier, 2016).

2. Materials and Methods

2.1. Materials

Industrially produced oxidative sintered pellets were sampled at five different FeCr smelters, with the associated sinter plants. These smelters/sinter plants requested to remain anonymous, and consequently, these operations will merely be referred to as Sinter Plants 1–5. Approximately 50 kg of sintered pellets were sampled at each sinter plant. As previously indicated, a fraction of sintered pellets is recirculated to protect the perforated stainless-steel belt used in the process. Considering this, it was ensured that the above-mentioned 50 kg of sintered pellets were subjected to a single sintering cycle.

Since the specific ores used to produce the above-mentioned oxidative sintered pellets were not available to the authors, six different chromite ores that were used as feedstock in sintering plants in South Africa were obtained as case study ores. Again, to retain anonymity, the considered ores are referred to as Ores 1–6. It is noted that the ores originated from various locations in the Bushveld Complex, as well as from various groups, and showcase the dissimilarities of the ores present therein.

2.2. Sub-Surface Characterization

From each of the five sinter plants (Sinter Plants 1–5), five pellets were selected at random. Each of the 25 pellets was halved and set in resin (Technoresin LR151 B:7). An SS20 Spectrum System Grinder polisher was used to grind the pellets to get rid of the excess resin and flatten the sample surface. A continuous water flow was maintained during grinding to clean and lubricate the grinding discs. Hereafter, the pellets were polished using 9, 3, and 1 μm of the DiaDuo-2 diamond paste suspension as a lubricant with soft polishing cloths. The grinder polisher operated at an average speed of 300 r/min for grinding and 150 r/min for polishing. During polishing, the diamond paste suspension poly lubricant was applied on the diamond paste cloths to obtain a mirror-like smooth polished surface.

The polished samples were C-coated using an Emscope C-coater. This was required before SEM analysis to ensure conductivity since the samples were set in resin. Surface analysis of the polished sample was conducted with an FEI Quanta 200 scanning electron microscope (SEM) with an integrated Oxford Instruments INCA 200 energy-dispersive X-ray spectroscopy (EDS) microanalysis system.

2.3. Chemical and Mineralogical Characterization

The chemical analyses of the chromite ore were conducted by performing inductively coupled plasma optical emission spectrometry (ICP-OES) on the samples, using a SPECTRO ARCOS SOP ICP-OES. Samples were solubilized using alkaline fusion by fusing 0.2 g of ore with 2 g of Na_2O_2 and 0.5 g of $NaCO_3$ in a tungsten crucible. The fused bead was then dissolved in a solution of 20 vol% HNO_3. Care was taken to ensure that the fused material dissolved and that there was no solid residue. Hereafter, the solution was subjected to ICP-OES analysis.

To determine the mineral compositions of the chromite ore samples, semi-quantitative X-ray diffraction (XRD) analyses were conducted. A Philips X-ray diffractometer (PW 3040/60 X'Pert Pro, Eindhoven, Netherlands) with Cu Kα radiation was used to perform the analyses. The measurements for the analyses were carried out between variable divergence and fixed receiving slits. The crystalline phases were identified using X'Pert Highscore plus software (Version 5.1, Malvern Panalytical, Malvern, United Kingdom), with the relative phase amounts being estimated using the Rietveld method (Autoquan program). Only the semi-quantitative crystalline phase composition obtained from XRD analysis was presented in this study to highlight the dissimilarities of the ores considered here.

2.4. Thermogravimetric Analyses

Commercially available TGA instruments can typically only handle a very small sample weight, which is far less than a single unoxidized chromite composite pellet. The objectives of this study could only be achieved if the surface and core properties of oxidative sintered pellets could be evaluated. Therefore, a custom-made large mass TGA was designed and commissioned for this study. For this purpose, a Lenton Elite, UK model TSH15/75/610 ceramic tube furnace was modified into the large-mass TGA. The samples were placed inside a crucible, which was then placed on top of a pedestal. The pedestal was attached to an alumina tube that rested on top of a scale. The scale was attached to a platform, which was raised to locate the sample-loaded crucible within the hot zone of the large-mass TGA. A stainless-steel flange was fixed to the top of the tube, which had a gas inlet port and a closed-end alumina tube in which a thermocouple was placed. The thermocouple was used to measure the temperature within the hot zone where the sample was located, which was also continuously logged. Mass measurements were logged using a high-sensitivity digital scale (Ohaus Explorer, EX2202; Sigma-Aldrich, South Africa). The furnace was heated at a rate of 5 °C/min from room temperature to 800 °C and thereafter at 10 °C/min from 800 °C to the desired temperature, i.e., 1350 °C for oxidative alteration and 1250 °C for reduction. These heating rates were chosen to protect the ceramic tube in the furnace from cracking (as per the manufacturer's guidelines). With this large-mass TGA, 20 composite pellets lying in a small "bed" could be evaluated per experiment, which more closely replicated the pellet bed inside the oxidative sintering process than what would be the case for the very small quantity of un-pelletized chromite composite in a commercial TGA.

During oxidative alteration experiments, the tube was continuously purged with air at a 1.2 sL/min flow rate. For reduction experiments, the same setup was used but the tube was purged with a 1.2 sL/min N_2, the sample inside the crucible was covered with graphite (representative of approximately 300% excess of C), and the crucibles were covered with a lid to ensure that the atmosphere within the crucible comprised CO/CO_2.

The large-mass TGA was evaluated against a commercial/research and development TGA to determine if it yielded similar results. For this, the same composite chromite pellet mixture was treated in both TGAs and the results were compared. The validation is presented in Section 3.1.

3. Results and Discussion

3.1. Validation of In-House Designed and Fabricated Large-Mass TGA

To determine if the large-mass TGA had comparable results to a commercial TGA, the same milled mixture of chromite, binder (i.e., bentonite clay), and reductant was treated in both TGAs. A total of 45 mg of the mixture was added to the commercial TGA, while 20 composite pellets were loaded into the large-mass TGA. The respective TGA curves are shown in Figure 3.

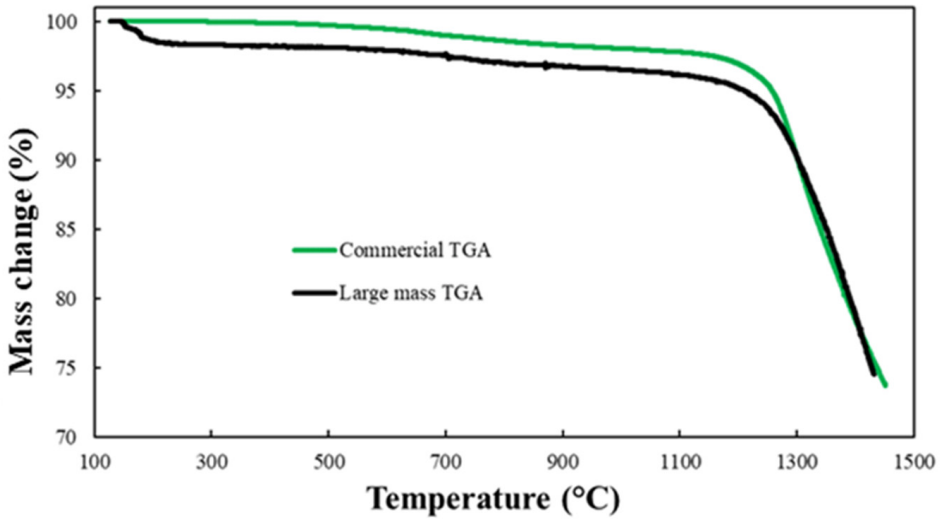

Figure 3. Comparison of TGA curves from a commercial/research TGA using a 45 mg composite pellet mixture and the large-mass TGA used in the study, loaded with 20 composite pellets with an approximate weight of 20 g. Both instruments were operated in a N_2 gas environment.

Figure 3 shows that both TGAs had comparable overall mass change %, which suggests that the large-mass TGA was fit for this purpose. The initial dissimilar mass change rates observed at approximately 150 °C may relate to the presence of moisture in the pelletized chromite, i.e., 45 mg of dry chromite powder was used for the commercial TGA and 20 composite pellets for the large-mass TGA. During the preparation of the 20 composite pellets, water was used to generate the green pellets. Hamad et al. (2024) and Ayari et al. (2005) stated that adsorbed and interlayer water is removed from bentonite at temperatures of up to ~130–150 °C [47,48]. Though the pellets were dried before TGA analysis, it is likely that some moisture was adsorbed by the bentonite clay binder and was only displaced at temperatures above 100 °C.

3.2. Characterizing the Extent of Oxidative Alteration of Industrially Sintered Pellets

The pellets obtained from Sinter Plants 1–5 were evaluated in terms of the depth of oxidative alteration. SEM micrographs of cross-sectional polished pellets from each of the sinter plants are presented in Figures 4–8. The micrographs were used to derive the semi-quantified oxidative alteration penetration depth into the pellets. Micrographs were taken every 0.5–1.5 mm, starting at the edge and moving toward the center of the pellet. These micrographs recorded the extent of oxidative alteration by identifying the light areas that represent the sesquioxide phases present in the Widmanstätten-like pattern, which signifies Fe liberation from the chromite spinel. Considering that it has been well established that the formation of the Widmanstätten pattern signifies oxidation of Fe^{2+} to Fe^{3+} [37,41–44], the presence thereof was used to measure the depth to which the pellets were oxidatively altered. Light grey areas indicated the bulk chromite. The dark grey particles were flux/binder/waste rock, while the black areas were the resin that was used for pellet mounting. Not all the SEM micrographs are presented here; instead, selected micrographs include representative images that best illustrate the observed characteristics

across the sinter plants. All micrographs were carefully selected to best represent the typical and relevant features. Therefore, only the representative samples from each of the relevant sinter plants (Sinter Plants 1–5) were presented. Since five pellets of each sinter plant were selected, the pellets were numbered Pellets 1–5. Each figure has a short description of observations made from the micrographs. The oxidative alteration depths are summarized in Table 1 in Section 3.3.

3.2.1. Sinter Plant 1 Pellets

Figure 4 presents the SEM micrographs of the oxidative pellets from Sinter Plant 1. Here, Figure 4a is used to show the phases present for all samples, i.e., the Fe_2O_3-enriched sesquioxide phase present in the Widmanstätten pattern, altered chromite, pellet binder, and voids within the pellets. These phases are not indicated for each of the micrographs, as only the presence or absence of the Widmanstätten pattern was of concern. Figure 4a,b shows the edge and center of Pellet 1, respectively. The edge of the pellet shows Fe oxidation phases within some of the pellet grains. Minute oxidative alteration occurred in the grains at the center of the pellet. As a minimum, it is expected that a typical sintered pellet has at least slight oxidative alteration on the pellet edges. Figure 4c,d shows the micrographs of Pellet 4 at the edge and in the center of the pellet, respectively. In this pellet, no visible signs of oxidative alteration can be seen at the pellet edge and center.

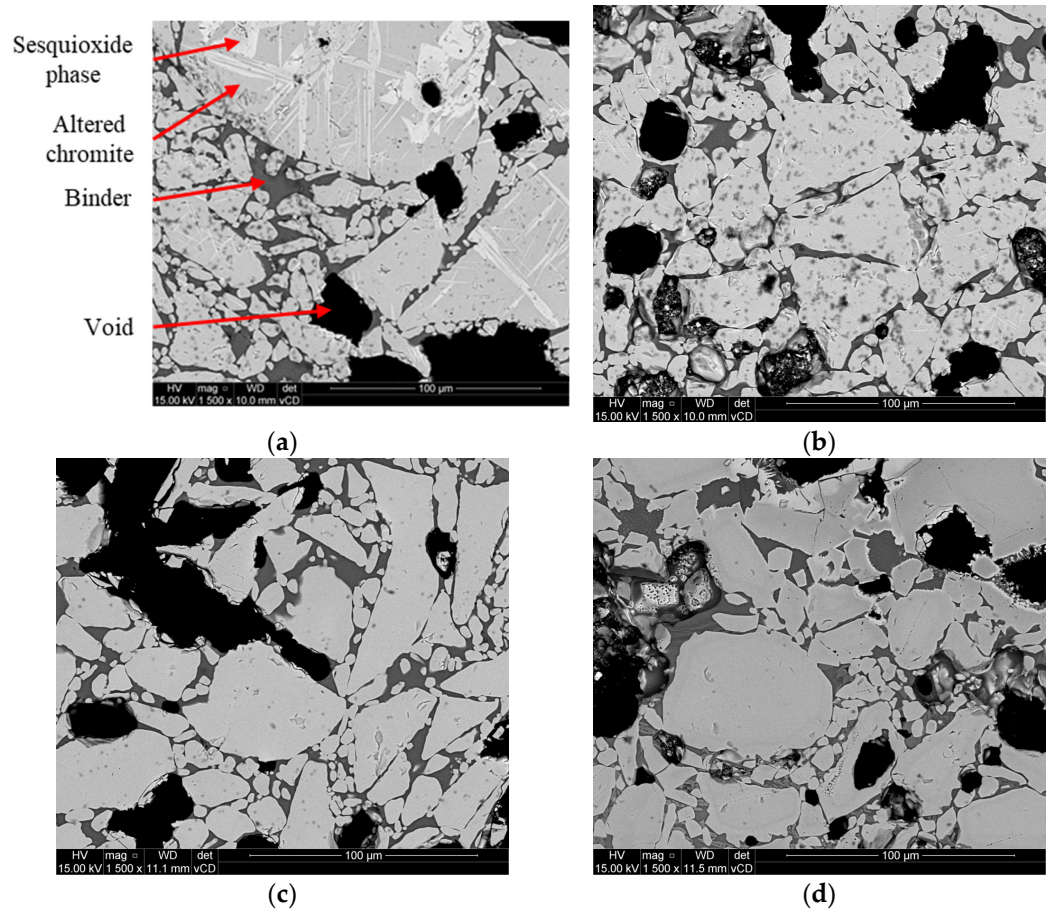

Figure 4. Backscatter electron SEM micrographs of Sinter Plant 1, Pellet 1, near the edge (**a**) and at the pellet center (**b**); Sinter Plant 1, Pellet 4, near the edge (**c**) and at the pellet center (**d**).

3.2.2. Sinter Plant 2 Pellets

Figure 5 presents the investigated pellets obtained from Sinter Plant 2. Figure 5a,b shows the micrographs of Pellet 2 at the edge and in the center of the pellet, respectively. Figure 5c,d shows the micrographs of Pellet 4. Pellet 2 showed no signs of oxidative alteration either at the edge or in the center of the pellet, while Pellet 4 showed oxidative alteration throughout the pellet.

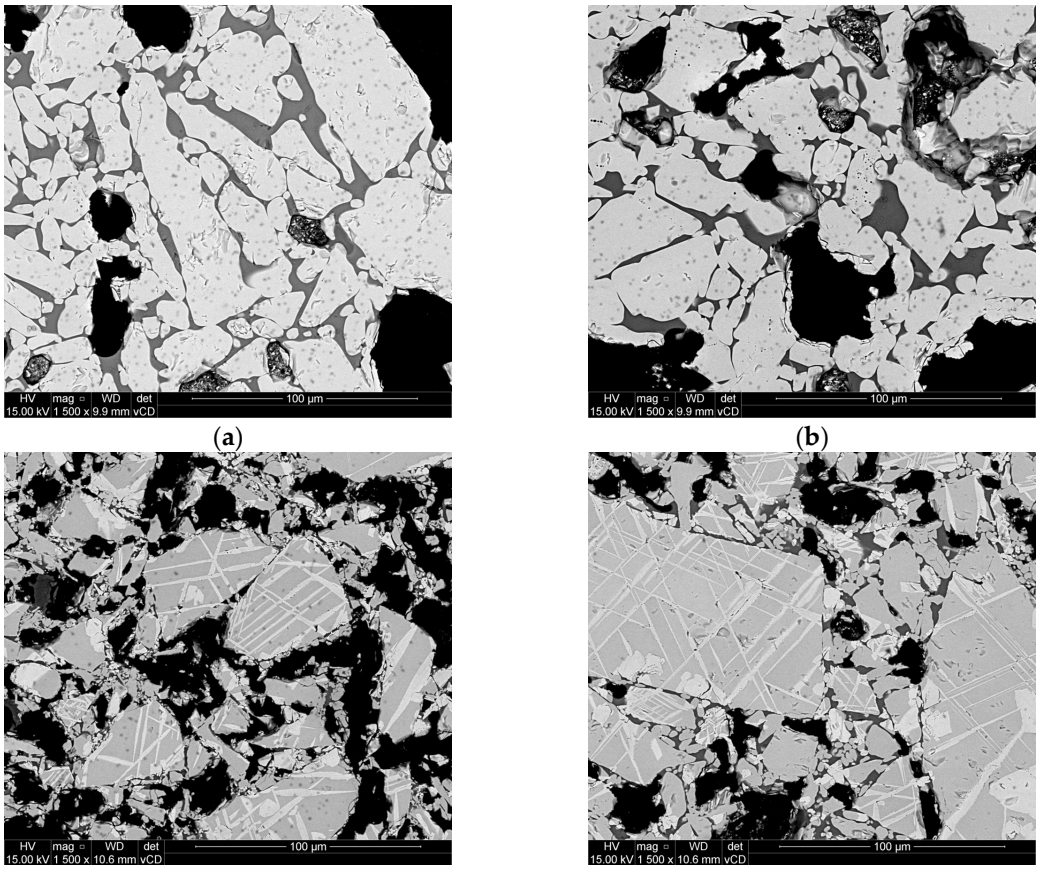

Figure 5. Backscatter electron SEM micrographs of Sinter Plant 2, Pellet 2, near the edge (**a**) and at the pellet center (**b**); Sinter Plant 2, Pellet 4, near the edge (**c**) and at the pellet center (**d**).

3.2.3. Sinter Plant 3 Pellets

Figure 6 shows the micrographs of two pellets from Sinter Plant 3. Figure 6a,b shows the edge and the center, respectively, of Pellet 2. No signs of oxidative alteration are visible in this pellet, either at the edge or at the center of the pellet. Pellet 3 shows signs of oxidative alteration at the edge of the pellet (Figure 6c), but no oxidative alteration in the center of the pellet (Figure 6d).

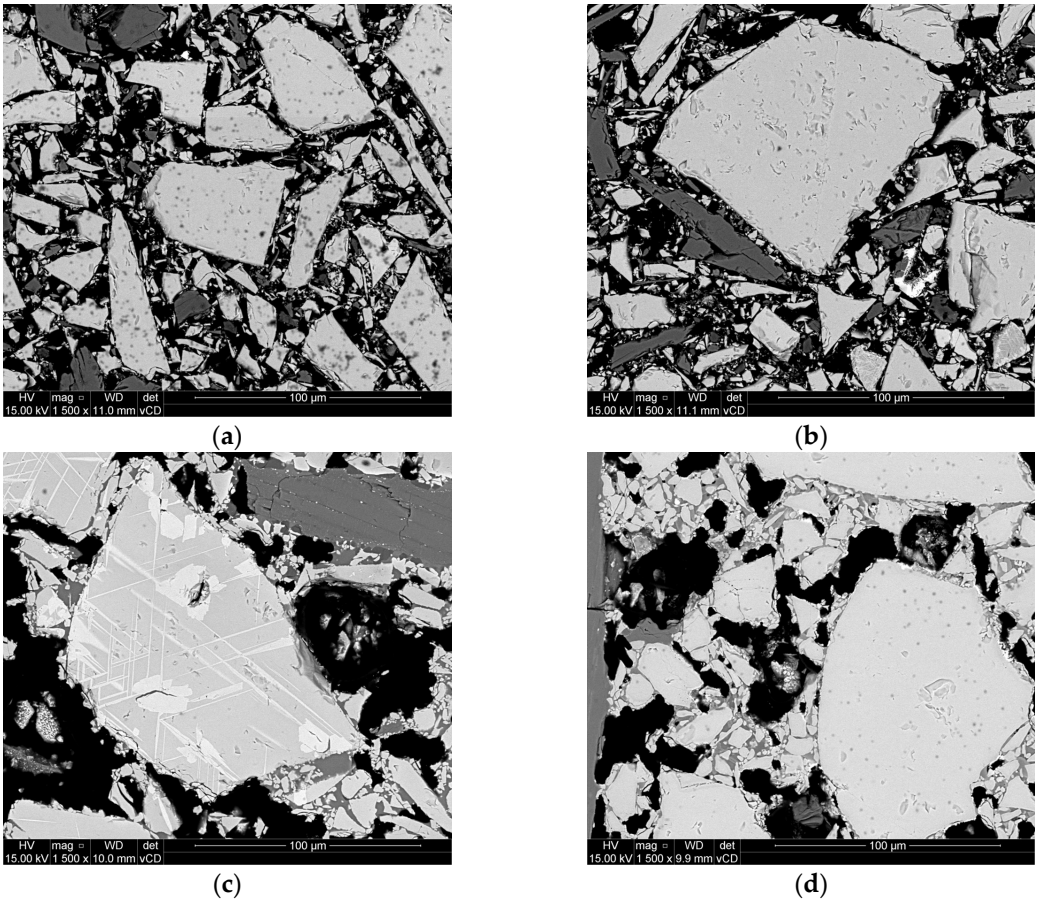

Figure 6. Backscatter electron SEM micrographs of Sinter Plant 3, Pellet 2, near the edge (**a**) and at the pellet center (**b**); Sinter Plant 3, Pellet 3, near the edge (**c**) and at the pellet center (**d**).

3.2.4. Sinter Plant 4 Pellets

Figure 7a–d presents micrographs of Pellets 1 and 3 from Sinter Plant 4. In Figure 7a, extensive oxidative alteration can be seen on all the grains at the edge of the pellet. In Figure 7b, minute oxidative alteration on some of the grains of the pellet can be observed. For Pellet 3, extensive oxidative alteration at the pellet edge was observed (Figure 7c), whereas slightly visible signs of oxidative alteration in the center (Figure 7d) of the pellet can be seen.

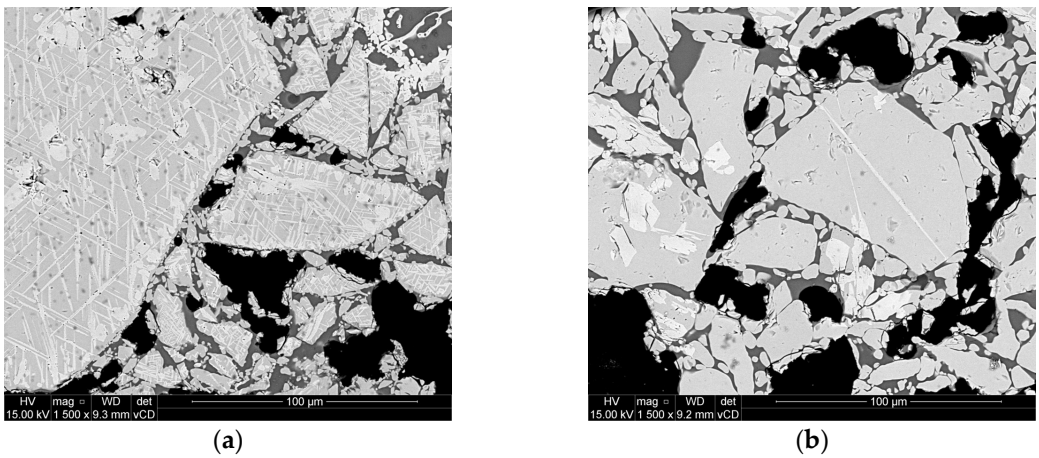

Figure 7. *Cont.*

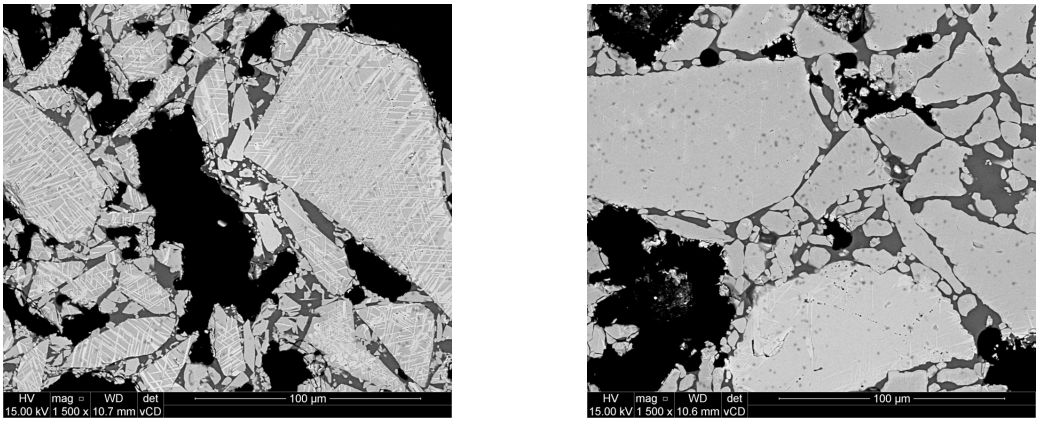

(**c**) (**d**)

Figure 7. Backscatter electron SEM micrographs of Sinter Plant 3, Pellet 1, near the edge (**a**) and at the pellet center (**b**); Sinter Plant 3, Pellet 3, near the edge (**c**) and at the pellet center (**d**).

3.2.5. Sinter Plant 5 Pellets

Figure 8 presents micrographs of the case study Pellet 1 in Sinter Plant 5. Only one pellet is shown here as all grains present in all considered pellets showed extensive oxidative alteration.

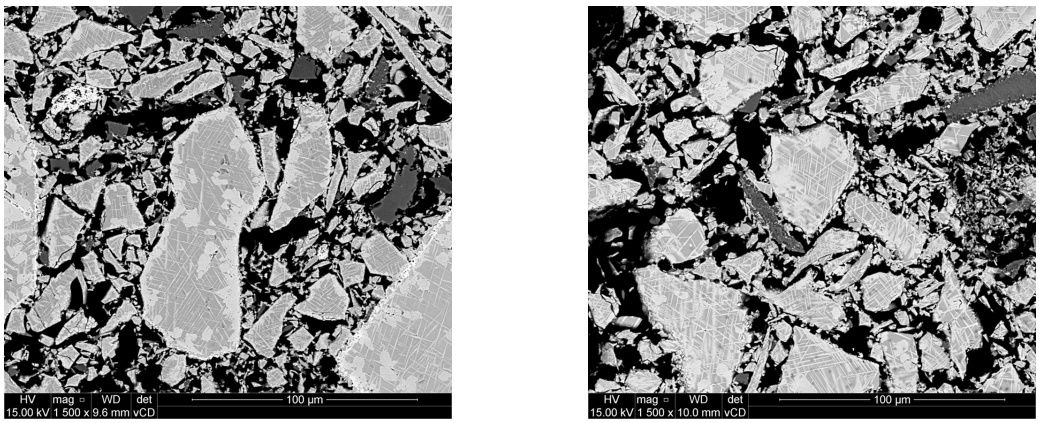

(**a**) (**b**)

Figure 8. Backscatter electron SEM micrographs of Sinter Plant 5, case study Pellet 1 near the pellet edge (**a**) and at the center (**b**).

3.3. Summary of Oxidative Alteration of Sintered Pellets and Probable Causes Therefore

The observations made from the cross-section and micrographed oxidatively sintered pellets from the various sinter plants presented in Section 3.2. are summarized in Table 1. This table also presents pellets not presented in Section 3.2.

Table 1. The semi-quantitative percentage oxidative alteration penetration depth calculated from five representative pellets from each of the five industrial sintering plants.

Sinter Plant	Pellet Number	Pellet Radius (mm)	Oxidative Alteration Depth (mm)	Oxidative Alteration Penetration (%)	Average Oxidative Alteration Penetration (Avg.% ± Std. Dev.)
1	1	7.00	5.85	83.6	20.1 ± 35.8
	2	6.75	0.62	9.2	
	3	6.50	0.49	7.5	
	4	6.50	0.00	0.0	
	5	6.50	0.00	0.0	

Table 1. *Cont.*

Sinter Plant	Pellet Number	Pellet Radius (mm)	Oxidative Alteration Depth (mm)	Oxidative Alteration Penetration (%)	Average Oxidative Alteration Penetration (Avg.% ± Std. Dev.)
2	1	7.00	7.00	100.0	43.9 ± 51.4
	2	7.00	0.00	0.0	
	3	6.50	0.74	11.4	
	4	7.00	7.00	100.0	
	5	7.00	0.56	8.0	
3	1	6.25	0.00	0.0	8.9 ± 11.4
	2	7.00	0.00	0.0	
	3	6.25	1.37	21.9	
	4	6.75	1.41	20.9	
	5	6.25	0.12	1.9	
4	1	6.25	6.25	100.0	94.0 ± 13.4
	2	6.75	6.75	100.0	
	3	6.75	4.72	69.9	
	4	7.25	7.25	100.0	
	5	6.50	6.50	100.0	
5	1	6.75	6.75	100.0	100.0 ± 0.0
	2	6.75	6.75	100.0	
	3	6.25	6.25	100.0	
	4	6.25	6.25	100.0	
	5	6.75	6.75	100.0	

From Table 1, the pellets from the various sinter plants had comparable diameters, i.e., 6.66 ± 0.29 mm. Therefore, the effect of pellet diameter on the effect of oxidation can be disregarded for the pellets considered from Sinter Plants 1–5. Nevertheless, Sinter Plants 1–3 produced pellets with poor oxidative alteration penetration (8.9%–43.9%), whereas Sinter Plants 4 and 5 produced highly (Sinter Plant 4, 94%) or fully (Sinter Plant 5, 100%) oxidatively altered pellets. In addition to the oxidative alteration penetration, the deviations are also considered indicators. For pellets from the same sinter plant, a large deviation in oxidative alteration penetration suggests inconsistent pellet sintering. When considering the deviations of 35.8 and 51.4% observed for Sinter Plants 1 and 2, respectively, the sintered pellets from the same plants differ significantly. The opposite is true for Sinter Plant 5, which had 0% deviation for the considered pellets, suggesting that pellets produced from this plant are highly consistent.

Table 1 further suggests that sinter plants essentially operating on similar technology and operational mandates produce pellets with vastly different extents of sintering. In addition to this, pellets produced by the same sinter plant may also differ significantly, e.g., pellets with oxidative alteration depths of 0%–100% for Sinter Plant 2. To better understand the inconsistency in the extent of oxidative alteration penetration, the sintering process is considered to identify possible operational parameters that may affect oxidative alteration.

As indicated in Section 1, green pellets are carried through a multicompartment sintering furnace on a perforated steel belt and heat is provided by the combustion of fuels such as coke breeze or CO(g). The green pellets are exposed to increasingly higher temperatures as they progress through the sinter plant, undergoing a wide variety of chemical, compositional, and mechanical changes.

Leipold and Zietsman (2014) modeled the temperature distribution of the sintering process using the process shown in Figure 9a using a wide range of variables, of which some are mentioned here [49]. The first compartment, i.e., the drying zone, is designated to evaporate water from the green pellets and operates at approximately 420 °C. Hereafter, the pellets move toward a heating zone (approximately 1150 °C) before entering the sintering zone (1250 °C). Hereafter, the pellets entered the cooling zones. The pellet bed layer was

as follows: 260 mm of green pellets layered onto a 190 mm layer of pre-sintered pellets. For the model, the length of the zones was as follows: a 5500 mm drying zone, 4000 mm for both the heating and sinter zones, and 2920 mm for the balancing zone [49]. The authors noted that their model does not consider C combustion, water evaporation, and the oxidation/reduction of Fe-oxides during the sintering process. Nevertheless, the C present in the green pellets is ignited in the sintering zone and is allowed to combust as the pellets progress through a so-called balancing zone [50]. Hereafter, the sintered pellets pass through various cooling zones and are stockpiled for down-steam smelting. The associated temperature distribution, as modeled by Leipold and Zietsman (2014), is shown in Figure 9b. The values shown are the minimum, average, and maximum modeled temperatures [49].

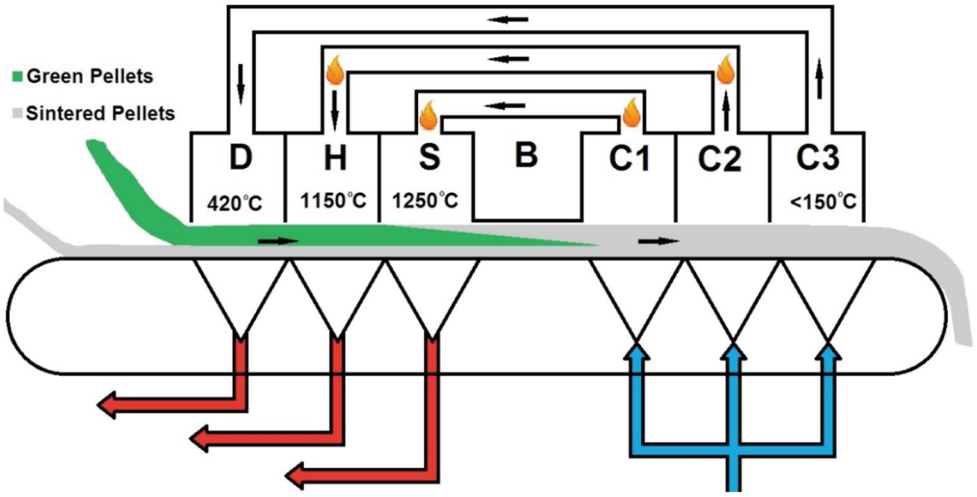

(**a**)

25 °C 1600 °C

	Drying			Heating			Sintering			Balancing			Cooling 1			Cooling 2			Cooling 3		
Furnace hoods	224.1			1149.3			1565.4						1109.4			656.9			224.2		
Green top layer	52	155	207	299	650	902	947	1146	1304	1302	1303	1304	1278	1103	910	868	647	450	414	218	90
Sintered bottom layer	27	99	167	489	503	670	585	760	942	940	941	942	885	632	428	395	257	151	135	69	35
Wind boxes	97.1			341.2			754.3						25.0			25.0			25.0		

(**b**)

Figure 9. The overall sinter process and the process used to model temperature distribution (D, drying; H, heating: S, sintering; B, balancing; C1–3, cooling) (**a**) and resulting temperature distribution (**b**) [49] (reused under license Creative Commons Attribution (CC BY)).

Figure 9a shows a schematic of the sintering process, with the relevant zones indicated in the caption. Figure 9b shows the temperature values at the top of the green pellet layer and the bottom of the sintered pellet layer. Based on this model, a relatively large temperature gradient (ΔT) exists between the pellet layer's top and bottom. For instance, the ΔT values for the heating, sintering, and balancing zones are 147, 386, and 362 °C, respectively, for the modeled average temperature values. Therefore, an appreciable ΔT exists between the top of the green pellet layer and the bottom of the pre-sintered pellet layer. Thus, it can be accepted that limited, if any, oxidative alternation will occur if the temperature at the bottom of the pellet layer is below the temperature required for this alteration.

Figure 9b further shows the dynamics of the green pellet layer and the proposed changes the layer undergoes during its exposure to the various zones, i.e., green pellets dry from top to bottom as they move through the sintering plant. As the top pellets dry, the hot gas becomes humid. For the pellets to be dried, the water vapor pressure should be less

than the saturation water vapor pressure. This is mainly dependent on the gas temperature. The gas temperature decreases as it moves towards the bottom of the pellet layer while concurrently becoming more humid. Therefore, the drying ability of the gas is reduced due to this decrease in gas temperature and increase in humidity [50].

The drying ability of the gas is based on the heat transfer between the gas and the pellets. The heat transferred between hot gas and pellets is assumed to follow Equation (2) [49,50]:

$$Q = hv\,(T_g - T_p) \quad (2)$$

where Q is the heat transferred, h is the heat transfer coefficient between the gas and pellets, v is the surface area where heat transfer occurs, and T_g and T_p are the temperatures of the gas and pellets, respectively. Hekkala et al. (2004) stated that h can be determined if the total pellet area in a certain volume in the pellet bed and the temperature difference between the pellet and gas are known [50]. However, h can range between 15 and 90 $kW{\cdot}m^{-2}.K^{-1}$ in a temperature range of 25 to 1500 K and at drying gas velocities of 0.4 to 1.2 $m.s^{-1}$. The heat transferred will nevertheless initially be consumed in three stages: (i) heating the pellet moisture to the boiling point, (ii) vaporizing water at the boiling point, and (iii) heating the evaporated water to the gas temperature. Therefore, the heat loss due to water vapor results in the heat transfer between the gas and pellets being dynamic, as suggested by the large pellet bed ΔT.

As previously mentioned, FeO liberated from the chromite spinel (E1) is oxidized to the sesquioxide phase Fe_2O_3, which requires the presence of oxygen. Considering that the sintering and balancing zones are the hottest zones, these are also the zones where Fe oxidation will occur. Keihäs et al. (2007) showed an appreciable decrease in the gas oxygen content in the sintering and balancing zones because of C combustion [51]. If the atmosphere is oxygen-starved, Fe oxidation may be limited, regardless of temperature. However, as shown in Figure 9b, air is introduced to the hot pellet layer at the first cooling zone. Here, the hot pellet layer (modeled at 1103–632 °C, top to bottom) is briefly exposed to air, during which Fe oxidation should occur toward the top of the pellet layer as the temperature would be sufficient for oxidation. As the pellets enter the second cooling zone, the temperature decreases (modeled at 647–257 °C, top to bottom) and the conditions for Fe oxidation are no longer sufficient. Therefore, if insufficient oxygen is present in the sintering and balancing zones, either due to insufficient airflow or excessive C content present in the pellets, Fe-oxidation will be limited, and only some oxidation may occur in the first cooling zone.

In summary, Table 1 shows that sintered pellets obtained from various sintering plants, operating on similar technology, do not yield pellets with comparable oxidative alteration depths. Moreover, even pellets from the same sinter plant also showed large deviations. It was theoretically demonstrated that pellet sintering and oxidative alteration are affected by numerous factors, e.g., pellet layer temperature, the heat transfer between the gas and pellets, and the presence of oxygen in the gas. From an operational point of view, process control may be varied to ensure the extent and consistency of pellet oxidative alteration. It is proposed that due to the various factors affecting pellet sintering and the dynamic nature of such factors, one would need to recover pellets from the top and bottom of the sintered pellet layer (excluding the pre-sintered pellet layer) after a single sintering run and determine if the employed process parameters are sufficient for acceptable oxidative alteration. Sinter Plant 5 may be taken as an example of an optimally operated sinter plant for the respective chromite ore as the pellets produced here are consistently fully oxidatively altered.

3.4. Ore Characterization and Oxidation Behavior

Excluding all oxidative sintering operational parameters, Leipold and Zietsman (2014) highlighted that the mineral composition may have an appreciable impact on the heating and cooling dynamics of the pellet bed as the various mineral phases present in the ore have different heat capacities [49]. However, Young and See (1976) stated that the difference

in chemical composition of the two chromite ores did not have a significant effect on the thermal conductivity of the ores [52]. Considering the experimental setup used for oxidative alteration, i.e., large-mass TGA, a temperature gradient in the pellet bed is likely to be minute, if any. Therefore, it may be accepted that the oxidation behavior of the considered ores relates exclusively to the chemical composition of the material and not to the heat transfer between the ore and air.

As indicated in Section 2.1, the specific ores used to produce the oxidative sintered pellets were not available to the authors and therefore six different chromite ores were obtained from different chromite mines in South Africa. In the following section, these ores were characterized and used in further analyses. Table 2 presents the ICP-OES chemical characterization of the six above-mentioned ores. The chromite ores have a Cr_2O_3 that ranges from 41.96% to 45.37% and FeO contents ranging from 23.53% to 26.99%. The Cr/Fe ratio ranges from 1.39 to 1.6, typical for South African chromite ore [20]. Table 3 presents the XRD analysis of the six ore samples, with wt% of phases determined using Rietveld refinement. Here, the primary focus was on investigating the oxidative behavior of chromite ores sourced from various mines in South Africa, with specific attention given to the variation in mass gain during oxidation. While the oxidation process inevitably results in changes in the phase composition of the material, a detailed post-oxidation phase analysis was not within the scope of this research.

Table 2. Chemical characterization of the ores obtained from ICP-OES analysis.

Species	Chromite Ore					
	1	**2**	**3**	**4**	**5**	**6**
Cr_2O_3	42.89	42.17	43.78	45.37	43.51	41.96
Fe_{tot} as FeO	23.53	26.76	24.98	26.99	24.24	26.50
SiO_2	4.62	3.88	2.81	0.94	5.36	3.95
Al_2O_3	13.92	16.77	14.64	15.18	14.57	16.44
MgO	11.83	7.27	10.33	9.41	10.58	7.13
CaO	0.43	0.63	0.12	0.13	0.19	0.62
TiO_2	0.54	0.67	0.69	0.78	0.66	0.67
MnO	0.21	0.20	0.22	0.22	0.19	0.20
Cr/Fe	1.60	1.39	1.54	1.48	1.58	1.39

Table 3. Semi-quantitative crystalline phase composition obtained from XRD analysis.

Phase	Formula	Chromite Ore					
		1	**2**	**3**	**4**	**5**	**6**
Chromite	$(Mg, Fe^{2+})(Al, Fe^{3+}, Cr)_2O_4$	4.3	38.3	81.8	87.7	72.6	
Magnetite	Fe_3O_4 (Fe^{3+}, Fe^{3+}, Fe^{2+})	1.3	2	1.8		0.7	17
Dolomite	$CaMg(CO_3)_2$	7.3					
Magnesioferrite	$Mg(Fe^{3+})_2O_4$	10.7	35.4		2	14.4	
Trevorite	$Ni^{2+}(Fe^{3+})_2O_4$	2.1	5.3		8.7	9.4	
Magnesiochromite	$MgCr_2O_4$	64.2	18.2	7.5		1.7	65.6
Ilmenite	$(Fe^{2+})TiO_3$		0.5	0.3	1.2	0.4	0.5
Hematite	Fe_2O_3	1.1	0.3	1.1	0.5	0.8	0.9
Diopside	$MgCaSi_2O_6$	9.1		7.5			16

To characterize the oxidation behaviors of the various ores, the large-mass TGA was used to record the mass change in the investigated ores as a function of temperature. Figure 10 presents the increase in mass as a function of temperature for the six case study ores. Figure 10a shows the average mass gained as a solid line, while the shaded areas indicate the standard deviation of mass gain. Figure 10b shows the same curves but for a larger temperature range, and the standard deviation was excluded.

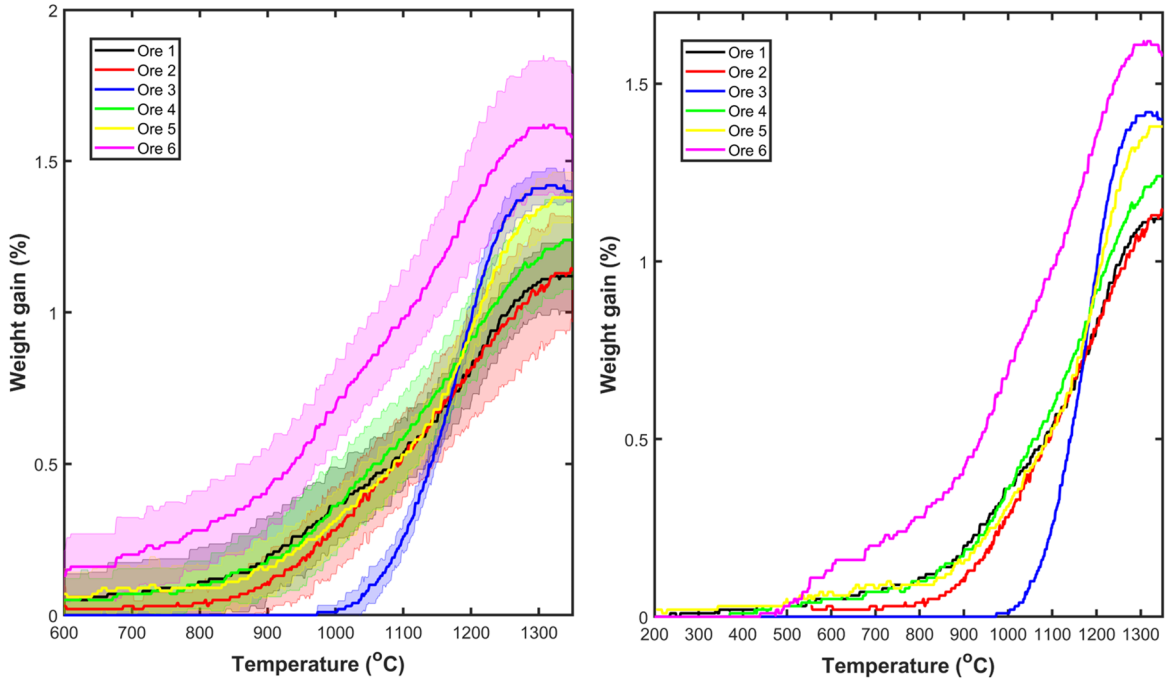

Figure 10. Average (solid lines) percentage mass gained with standard deviations (indicated by the lighter semi-transparent areas), measured with TGA, based on five measurement repeats for each case study ore (**a**). Same results as in Figure 10a, but without the standard deviations indicated and over a slightly large temperature range to make differences between the case study ores more apparent (**b**).

Figure 10a shows that the repeatability of measurements had a relative degree of deviation and that the difference between some ores was statistically significant. For instance, Ore 6 had a relatively large deviation, suggesting that the ore is not as homogenous as, for instance, Ore 3, which had a narrow deviation.

Figure 10b shows that the temperature at which mass gain was initiated for most ores ranged between 450 and 800 °C, whereas Ore 3 was initiated at approximately 980 °C. The mass gains became appreciable within approximately 100–350 °C of their initiation temperatures. When referring to Figure 9b, the average modeled temperatures at the top of the green pellet layer in the sintering and balancing zones are 1146 and 1303 °C, respectively. These temperatures would be sufficient for all chromite ores to undergo oxidative alteration, assuming sufficient oxygen contents are present during pellet sintering. However, when considering that the bottom of the pellet layer in the same zones are 760 and 941 °C, most of the considered ores would likely show signs of initial/partial oxidative alternation, while only Ore 6 would likely be fully altered. In addition, the oxidation rates would also play a determining role in the extent of oxidation. Sufficient retention times of ore within the sintering and balancing zones should afford high degrees of oxidation, at the cost of lower sintered pellet output.

The average mass gain ranged between 1.2 and 1.6 wt%, with Ore 6 showing the largest mass gain and Ores 1 and 2 the smallest. Most of the ores showed comparable mass gain rates, except Ore 3, which showed a more rapid mass gain. The oxidation behavior of the various ores may be discussed based on their compositions. The following observations may be made.

When considering that large and comparable fractions of Ores 1 (64.2 wt%) and 6 (65.6 wt%) comprise magnesiochromite, similar oxidation behavior may be expected. However, a relatively large mass gain was observed for Ore 6 when compared to Ore 1. The primary difference between the composition of Ores 1 and 6 was that Ore 6 contained 17 wt% magnetite (which contains a Fe^{2+} cation). Therefore, the dissimilar mass gain may be ascribed to the oxidation of Fe^{2+} to Fe^{3+} present in magnetite. Tang et al. (2024)

showed mass gains of four pelletized ferrous materials during oxidation. The mass gain of these materials, which ranged between ~0.6 and 2.5 mass% when oxidized at 1000 °C, was ascribed to the presence of FeO content and oxidizable oxides in each of the materials. Additionally, for all four materials, the ratio of Fe^{2+}/Fe^{3+} approached 0 as the oxidation temperature approached 1000 °C [53].

Ore 3 is comprised mainly of chromite (81.8 wt%), and magnesiochromite (7.5 wt%). Both phases are considered highly resistant to oxidation. The only constituent of chromite susceptible to oxidation at the investigated temperatures is the Fe^{2+} content thereof. Therefore, it may be assumed that the large chromite content affords Ore 3 its resistance against oxidation.

When jointly considering Ores 1, 2, 4, and 5, there is a significant difference in their phase compositions. The ores showed comparable mass gain rates and initiation temperatures. The main difference was the total mass gained, which may be ascribed to the dissimilar composition and was likely due to the presence of various amounts of Fe^{2+}-containing material.

The study by Biswas et al. (2018) showed that two ores of Indian origin had vastly different oxidation behaviors, both in terms of oxidation extent (defined as measured weight gain as a function of theoretical weight gain) and behavior at 700, 800, and 1000 °C. For instance, one of the ores showed varying degrees of oxidation at the different investigated temperatures, while the other ore showed consistent degrees of oxidation across all three investigated temperatures [43]. Ultimately, the dissimilar oxidation behavior of the investigated ores cannot be ascribed to a single property, other than dissimilar chemical and mineralogical composition. Due to the stochastic nature of the considered ores' composition, as a function of its point of recovery, ascribing mass gain to a single property/compound would be difficult. It is, however, understood that the oxidation of lower metal oxides is the most likely reason for mass gain; specifically, the oxidation of Fe^{2+} to Fe^{3+}. A recent study by Swanepoel and Garbers-Craig (2023) stated that chromite oxidation followed three stages: (i) Fe^{2+} oxidation in tetrahedral sites between 673 and 973 K, (ii) diffusion of Fe^{3+} octahedral to tetrahedral sites between 973 and 1173 K, and (iii) Fe^{3+} diffusion from tetrahedral to octahedral sites [41]. Therefore, it is worth investigating the Fe speciation of the various chromite ores before sintering to predict oxidation behavior during sintering. Moreover, the establishment of the extent of Fe oxidation relative to the before and after Fe^{2+}/Fe^{3+} ratio would be a valuable research perspective.

3.5. Metallurgical Benefit of Smelting Oxidatively Altered Chromite

This study aimed to showcase the metallurgical benefit associated with the oxidation of chromite pellets. For this investigation, Ore 3 was considered for two reasons: (i) it showed the highest initial resistance toward oxidation (i.e., mass gain initiated at approximately 980 °C), suggesting it was the most thermally stable of the various investigated ores, and (ii) it showed a relatively high mass gain of ~1.6 wt%, which is believed to be an indication of a high degree of Fe liberation and subsequent oxidation.

For this investigation, 10 pellets (~30 g) were prepared with unoxidized chromite, referred to here as the base case, and 10 pellets (~30 g) were prepared using oxidatively altered ore. As described in Section 2.4, the TGA was purged with N_2, and the crucible containing the C-covered pellets was closed with a lid. This approach ensured a CO/CO_2 atmosphere within the crucible similar to process gas formation within an SAF. Figure 11 presents the weight loss as a function of temperature. Six repeats of each sample were performed. Figure 11 shows the average of the six repeats as a solid line and the surrounding colored areas as the standard deviation.

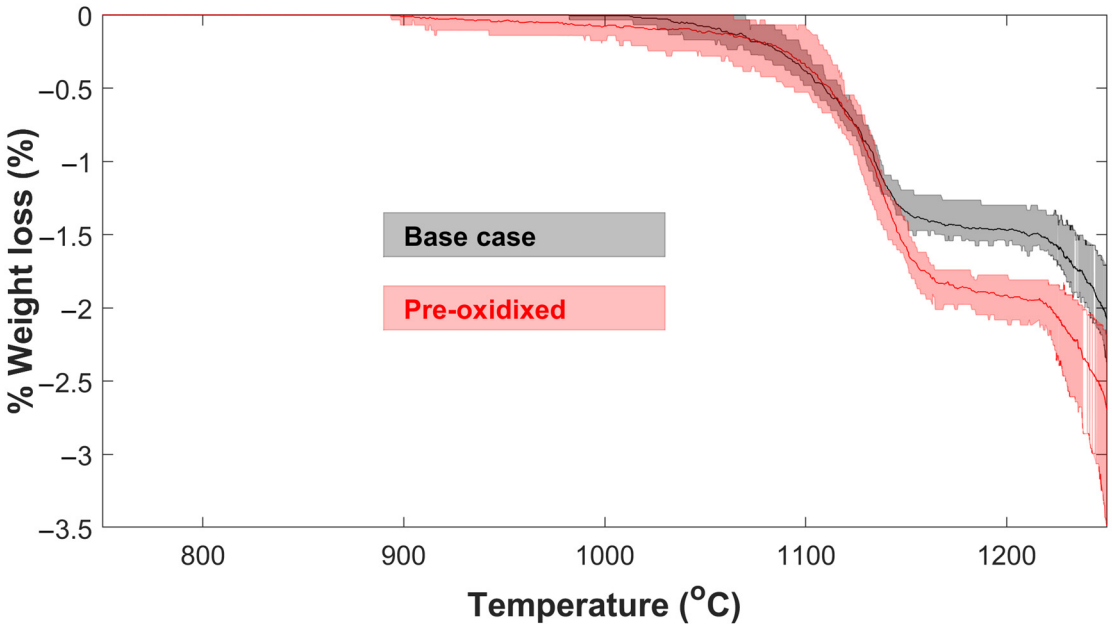

Figure 11. TGA curves of base case and sintered pellets.

Figure 11 shows that there was an appreciable difference in the mass change for the two considered pellet types. The negative mass change, i.e., mass loss, of the sintered pellets was initiated at approximately 900 °C, whereas the base case was initiated at 1020 °C. Hereafter, both pellet types showed comparable mass losses up to 1130 °C, i.e., 1.4 wt%. The oxidatively altered pellets showed a continuation of mass loss of up to 1.9 wt%. In both cases, the mass loss plateaued up to approximately 1250 °C, where it is expected that chromite metallization was initiated (as shown in Figure 2). Ultimately, the base case and oxidatively altered pellets had a total mass loss of approximately 2.0 and 2.5 wt%. Therefore, there was a 25% mass loss increase for the oxidatively altered pellets when compared to the base case pellets, which signifies the advantage of chromite's oxidative alternation during the oxidative sintering process. This suggests that a smelter consuming the sintered ore would require less energy to smelt the sintered ore when compared to non-oxidized ore. This translates into a relatively significant metallurgical benefit for the relevant smelter.

To signify the benefits of optimal pellet sintering (and the associated oxidative alteration), a study by Kleynhans et al. (2017) stated that chromite pre-oxidized at 1000 °C resulted in an increase in subsequent pre-reduction of 8.5%. This decreased the SEC by approximately 8.3%, reducing it from 2.4 to 2.2 MWh/t. Additionally, the carbonaceous material required for something decreased by roughly 14%, from 99.5 kg/t pellets to 85.5 kg/t pellets [54].

The metallurgical benefit of oxidatively altered chromite pellets therefore extends beyond only achieving increased Fe liberation. The pre-oxidation process enhances the reducibility of Fe-oxides, ensuring more efficient recovery during downstream smelting of both Fe and Cr. Improved recovery translates to higher FeCr yields and lower Cr losses. Furthermore, pre-oxidized chromite is critical in reducing the SEC during downstream smelting as pre-oxidized chromite consumes less energy, effectively reducing operation costs.

In summary, oxidatively altered chromite offers multiple benefits, e.g., improved metal recovery and lower Cr losses, and potential energy savings during smelting processes. These advantages highlight the importance of fully optimizing the respective sintering processes to ensure that chromite is fully pre-oxidized.

4. Conclusions

From the results presented, it is evident that sintered pellets produced by various South African sinter plants yielded pellets with largely varying degrees of chromite oxidation. A semi-quantitative method to determine oxidation was presented here, which showed that the oxidation depth varied between 8.9% ± 11.4 and 100% ± 0%. Similarly, pellets produced by the same plant could also vary significantly as deviations in the oxidation depth ranged between 0% and 51.4%. This variability underscores the critical role of operational parameters in determining the quality of oxidative sintering, even within plants employing similar technology and operational parameters. These findings provide new insights into the importance of maintaining consistent operational conditions to optimize pellet quality.

Individual ores were subjected to oxidation, and their mass gain, which is an indicator of oxidation, was measured. The mass gain for the ores ranged between 1.2 and 1.6 wt%. The temperature at which mass gain was initiated ranged between 450 and 930 °C, suggesting that the various ores had significantly dissimilar oxidation behaviors. These observations were ascribed to the different chemical and mineralogical compositions, further highlighting the need to monitor produced pellets to ensure optimal oxidation. Nevertheless, due to the wide range of compositional differences between ores, further investigation is required to disseminate the effect of the various phases on the oxidation behavior.

It was also shown that the mass loss, which is an indication of oxygen removal, during the solid-state reduction in oxidatively altered and non-oxidized was greater for the altered ore. The oxidatively altered ore showed a 25% increase in mass loss when compared to the non-oxidized ore. This difference translates into a greater degree of metallization. Thus, the metallurgical benefit of smelting oxidized ore is the lower energy consumption requirement. This energy-saving aspect, demonstrated through mass loss comparison, presents a clear operational advantage for FeCr producers seeking a more efficient and cost-effective smelting process.

From the presented results, it is evident that not only operational differences, e.g., differences in temperatures of the various sintering furnace compartments, but also the ability of ores to be oxidized (indicated as the liberation of Fe-oxides from the chromite spinel considered in this work), are likely to influence the metallurgical benefit that can be derived from smelting oxidative sintered pellets to produce FeCr. The variability in oxidation potential across different ores, as highlighted in this study, underscores the importance of optimizing both operational conditions and ore selection to maximize energy efficiency in smelting. The ability of ores to be oxidatively altered is particularly important if a variety of ores are used, as is the case for South African FeCr producers.

One prospect would be to develop a method to quantify chromite's oxidation post-sintering and pre-smelting. For instance, pellets could be recovered after sintering and rapidly heated to 1300 °C in air, and their mass gain could be determined. A zero-mass gain would suggest full oxidation. Alternatively, sintered pellets could be cross-sectioned, the cross-sectioned particles could be digitalized (either optically or by SEM), and a fit-for-purpose color recognition program could be used to quantify the degree of oxidation penetration. Developing such methods for rapid post-sintering oxidation assessment could provide a valuable tool for real-time quality control (in terms of oxidative alteration), ensuring consistent pellet quality and maximizing smelting efficiency.

Author Contributions: Conceptualization, J.P.B.; data curation, Y.v.S. and J.G.; formal analysis, Y.v.S., S.P.d.P. and J.G.; funding acquisition, J.P.B.; investigation, Y.v.S.; methodology, Y.v.S., J.P.B., P.G.v.Z. and J.G.; project administration, J.P.B.; resources, J.P.B. and P.G.v.Z.; software, Y.v.S.; spervision, J.P.B. and P.G.v.Z.; validation, S.P.d.P. and P.G.v.Z.; visualization, S.P.d.P.; writing—original draft, Y.v.S., S.P.d.P., J.P.B., P.G.v.Z. and J.G.; writing—review and editing, S.P.d.P., J.P.B. and P.G.v.Z. All authors have read and agreed to the published version of the manuscript.

Funding: This research was partially funded by industrial partners who opted to remain anonymous. Post-doctoral research funding for Y.v.S. was obtained from North-West University.

Data Availability Statement: Data are contained within the article.

Acknowledgments: The authors thank the ferrochrome smelters and chromite ore mines, who preferred to remain anonymous, for the sample materials.

Conflicts of Interest: The authors declare no conflicts of interest.

References

1. Goel, R. Smelting Technologies for Ferrochromium Production-Recent Trends. In *Ferro Alloy Industries in the Liberalized Economy*; NML: Jamshedpur, India, 1997.
2. Yu, D.; Paktunc, D. Carbothermic reduction of chromite fluxed with aluminum spent potlining. *Trans. Nonferrous Met. Soc. China* **2019**, *29*, 200–212. [CrossRef]
3. Steenkamp, J. Wear analysis of tap-holes at two ferrochromium production furnaces. *J. S. Afr. Inst. Min. Metall.* **2019**, *119*, 537–544. [CrossRef]
4. Pouroulis, P. International Chromium Development Association. Activity Report 2020. 2020. Available online: https://www.icdacr.com/wp-content/uploads/2022/10/ICDA_Activity_Report_2020.pdf (accessed on 31 October 2024).
5. Wei, J.-H.; Zhu, D.-P. Mathematical modeling of the argon-oxygen decarburization refining process of stainless steel: Part I. Mathematical model of the process. *Metall. Mater. Trans. B* **2002**, *33*, 111–119. [CrossRef]
6. Li, D.G.; Chi, H.B.; Shao, S.J. The Analysis of the Blowing Process with the Top Lance of the Argon Oxygen Decarburization (AOD) in Baosteel. In *Proceedings of the Materials Science Forum*; Trans Tech Publications: Stäfa, Switzerland, 2007; pp. 1039–1042.
7. Beukes, J.P.; du Preez, S.P.; van Zyl, P.G.; Paktunc, D.; Fabritius, T.; Päätalo, M.; Cramer, M. Review of Cr(VI) environmental practices in the chromite mining and smelting industry—Relevance to development of the Ring of Fire, Canada. *J. Clean. Prod.* **2017**, *165*, 874–889. [CrossRef]
8. Basson, J.; Daavittila, J. High carbon ferrochrome technology. In *Handbook of Ferroalloys*; Elsevier: Amsterdam, The Netherlands, 2013; pp. 317–363.
9. Ugwuegbu, C. Technology innovations in the smelting of chromite ore. *Innov. Syst. Des. Eng.* **2012**, *3*, 48–54.
10. Rao, V.; Singh, B. Turn around story at ferro alloy plant, Bamnipal. *Tata Techol.* **1996**, *23*, 7–14.
11. Singh, V.; Tathavadkar, V.; Rao, M.S.; Kumar, S. Estimating effect of chrome ore granulometry on sintered pellet properties. *Ironmak. Steelmak.* **2008**, *35*, 27–32. [CrossRef]
12. Naiker, O. The development and advantages of Xstrata's Premus Process. In Proceedings of the Eleventh International Ferroalloys Congress (INFACON XI), New Delhi, India, 18–21 February 2007; pp. 113–119.
13. Kleynhans, E.; Beukes, J.; Van Zyl, P.G.; Kestens, P.; Langa, J. Unique challenges of clay binders in a pelletised chromite pre-reduction process. *Miner. Eng.* **2012**, *34*, 55–62. [CrossRef]
14. Letaba, P.T.; Zulu, S. The development of a technology roadmap for ferrochrome producers. *S. Afr. J. Ind. Eng.* **2021**, *32*, 100–109. [CrossRef]
15. Dlamini, R.; von Blottnitz, H. Resource Intensity Trends in the South African Ferrochrome Industry from 2007 to 2020. *Minerals* **2022**, *13*, 44. [CrossRef]
16. Jones, R.T. DC arc furnaces—Past, present, and future. In *Celebrating the Megascale, Proceedings of the Extraction and Processing Division Symposium on Pyrometallurgy in Honor of David GC Robertson, TMS, San Diego, CA, USA, 17–20 February 2014*; Springer: Cham, Switzerland, 2016; pp. 129–139.
17. Berryman, E.J.; Paktunc, D.; Kingston, D.; Beukes, J.P. Composition and Cr-and Fe-speciation of dust generated during ferrochrome production in a DC arc furnace. *Clean. Eng. Technol.* **2022**, *6*, 100386. [CrossRef]
18. Agarwal, S.; Pal, J.; Ghosh, D. Smelting characteristics of fluxed chromite sinter and its performance assessment in electric arc furnace to produce high carbon ferrochrome. *Ironmak. Steelmak.* **2016**, *43*, 97–111. [CrossRef]
19. Riekkola-Vanhanen, M. *Finnish Expert Report on Best Available Techniques in Ferrochromium Production*; Finnish Environment Institute: Helsinki, Finland, 1999.
20. Nafziger, R.H. A review of the deposits and beneficiation of lower-grade chromite. *J. S. Afr. Inst. Min. Metall.* **1982**, *82*, 205–226.
21. Li, C.; Ripley, E.M.; Sarkar, A.; Shin, D.; Maier, W.D. Origin of phlogopite-orthopyroxene inclusions in chromites from the Merensky Reef of the Bushveld Complex, South Africa. *Contrib. Mineral. Petrol.* **2005**, *150*, 119–130. [CrossRef]
22. Hasch, M.; Latypov, R. Too large to be seen: Regional structures in Lower and Middle group chromitites of the Bushveld Complex, South Africa. *Ore Geol. Rev.* **2021**, *139*, 104520. [CrossRef]
23. Barnes, A.; Finn, C.W.P.; Algie, S. The prereduction and smelting of chromite concentrate of low chromium-to-iron ratio. *J. S. Afr. Inst. Min. Metall.* **1983**, *83*, 49–54.
24. Yudovskaya, M.A.; Kinnaird, J.A. Chromite in the Platreef (Bushveld Complex, South Africa): Occurrence and evolution of its chemical composition. *Miner. Depos.* **2010**, *45*, 369–391. [CrossRef]
25. Latypov, R.; Chistyakova, S.Y.; Letsoele, C. Massive chromitites of the Bushveld Complex, South Africa: A critical review of existing hypotheses. *Earth-Sci. Rev.* **2024**, *256*, 104858. [CrossRef]

26. Schurmann, E.; von Schweinichen, J. Investigation of the Melting Equilibria of Iron Rich, Ternary Fe--C--X sub i Alloys With X sub i= Aluminum, Copper, Nickel and Chromium. *Giessereiforschung* **1986**, *38*, 125–132.
27. Kinnaird, J.; Kruger, F.; Nex, P.; Cawthorn, R. Chromitite formation—A key to understanding processes of platinum enrichment. *Appl. Earth Sci.* **2002**, *111*, 23–35. [CrossRef]
28. Naldrett, A.; Wilson, A.; Kinnaird, J.; Yudovskaya, M.; Chunnett, G. The origin of chromitites and related PGE mineralization in the Bushveld Complex: New mineralogical and petrological constraints. *Miner. Depos.* **2012**, *47*, 209–232. [CrossRef]
29. Latypov, R.; Chistyakova, S.; Barnes, S.J.; Godel, B.; Delaney, G.W.; Cleary, P.W.; Radermacher, V.J.; Campbell, I.; Jakata, K. Chromitite layers indicate the existence of large, long-lived, and entirely molten magma chambers. *Sci. Rep.* **2022**, *12*, 4092. [CrossRef] [PubMed]
30. Dzvinamurungu, T.; Rose, D.H.; Viljoen, K.S.; Mulaba-Bafubiandi, A.F. A Process Mineralogical Evaluation of Chromite at the Nkomati Nickel Mine, Uitkomst Complex, South Africa. *Minerals* **2020**, *10*, 709. [CrossRef]
31. Langa, M.M.; Jugo, P.J.; Leybourne, M.I.; Grobler, D.F.; Adetunji, J.; Skogby, H. Chromite chemistry of a massive chromitite seam in the northern limb of the Bushveld Igneous Complex, South Africa: Correlation with the UG-2 in the eastern and western limbs and evidence of variable assimilation of footwall rocks. *Miner. Depos.* **2021**, *56*, 31–44. [CrossRef]
32. Glastonbury, R.I.; Beukes, J.; Van Zyl, P.; Sadikit, L.; Jordaan, A.; Campbell, Q.; Stewart, H.; Dawson, N. Comparison of physical properties of oxidative sintered pellets produced with UG2 or metallurgical-grade South African chromite: A case study. *J. S. Afr. Inst. Min. Metall.* **2015**, *115*, 699–706. [CrossRef]
33. du Preez, S.P.; van Kaam, T.P.M.; Ringdalen, E.; Tangstad, M.; Morita, K.; Bessarabov, D.G.; van Zyl, P.G.; Beukes, J.P. An Overview of Currently Applied Ferrochrome Production Processes and Their Waste Management Practices. *Minerals* **2023**, *13*, 809. [CrossRef]
34. Swanepoel, S.; Garbers-Craig, A.M.; De Villiers, J.P. The oxidation behavior of a selection of South African chromites. *Metall. Mater. Trans. B* **2022**, *53*, 3805–3824. [CrossRef]
35. Zhao, B.; Hayes, P. Effects of oxidation on the microstructure and reduction of chromite pellets. In Proceedings of the Twelfth International Ferroalloys Congress (INFACON XII), Helsinki, Finland, 6–9 June 2010; pp. 263–273.
36. Du Preez, S.P.; Beukes, J.P.; Paktunc, D.; Van Zyl, P.G.; Jordaan, A. Recycling pre-oxidized chromite fines in the oxidative sintered pellet production process. *J. S. Afr. Inst. Min. Metall.* **2019**, *119*, 207–215. [CrossRef]
37. Kapure, G.; Tathavadkar, V.; Rao, C.; Rao, S.; Raju, K. Coal based direct reduction of preoxidized chromite ore at high temperature. In Proceedings of the Twelfth International Ferroalloys Congress (INFACON XII), Helsinki, Finland, 6–9 June 2010; pp. 6–9.
38. Kleynhans, E.L.J.; Neizel, B.W.; Beukes, J.P.; van Zyl, P.G. Utilisation of pre-oxidised ore in the pelletised chromite pre-reduction process. *Miner. Eng.* **2016**, *92*, 114–124. [CrossRef]
39. Kleynhans, E.; Beukes, J.; van Zyl, P.; du Preez, S. Chemical beneficiation of chromite ore to improve the chromium-to-iron ratio for ferrochrome production. *Miner. Eng.* **2023**, *201*, 108196. [CrossRef]
40. Davies, J.; Tangstad, M.; Ringdalen, E.; Beukes, J.P.; Bessarabov, D.; du Preez, S.P. The Effect of Pre-Oxidation on the Reducibility of Chromite Using Hydrogen: A Preliminary Study. *Minerals* **2022**, *12*, 911. [CrossRef]
41. Swanepoel, S.; Garbers-Craig, A.M. Isothermal oxidation kinetics of industrial South African chromite concentrates in air. *Miner. Eng.* **2023**, *202*, 108263. [CrossRef]
42. Borra, C.R.; Kapure, G.; Tathavadkar, V. Investigation of pre-oxidation of Sukinda Chromite Ore. *Tata Search* **2010**, *1*, 145–148.
43. Biswas, A.; Konar, B.; Kapure, G.U.; Sahu, N.; Paliwal, M. Pre-oxidation treatment of Indian chromite ores: Kinetics and phase transformation behavior relevant to ferrochrome manufacturing and pelletization. *Miner. Process. Extr. Metall.* **2018**, *130*, 31–41. [CrossRef]
44. Pan, J.; Yang, C.; Zhu, D. Solid state reduction of preoxidized chromite-iron ore pellets by coal. *ISIJ Int.* **2015**, *55*, 727–735. [CrossRef]
45. Alper, A.M. *High Temperature Oxides, Part 1: Magnesia, Lime and Chrome Refractories*; Academic Press: New York, NY, USA, 1970.
46. Tathavakar, V.D.; Antony, M.; Jha, A. The physical chemistry of thermal decomposition of South African chromite minerals. *Metall. Mater. Trans. B* **2005**, *36*, 75–84. [CrossRef]
47. Ayari, F.; Srasra, E.; Trabelsi-Ayadi, M. Characterization of bentonitic clays and their use as adsorbent. *Desalination* **2005**, *185*, 391–397. [CrossRef]
48. Hamad, H.N.; Idrus, S.; Yusuf, B.; Jamali, N.S.; Ahsan, A.; Suhartini, S.; Wahab, A.M.A. Optimized Bentonite Clay Adsorbents for Methylene Blue Removal. *Processes* **2024**, *12*, 738. [CrossRef]
49. Leipoldt, W.; Zietsman, J. Modelling of a steel belt sintering process. In Proceedings of the Pyrometallurgical Modelling 2014, Rosebank, South Africa, 4–5 August 2014; pp. 147–156.
50. Hekkala, L.; Fabritius, T.; Härkki, J. Mathematical model of heat and mass transfer in the steel belt sintering process. In Proceedings of the Tenth International Ferroalloys Congress (INFACON X), Cape Town, South Africa, 1–4 February 2004; p. 4.
51. Keihäs, J.; Mäkelä, P.; Ollila, J.; Hekkala, L. CFD modelling of the steel belt sintering process. In Proceedings of the Eleventh International Ferroalloys Congress (INFACON XI), New Delhi, India, 18–21 February 2007; pp. 18–21.
52. Young, M.; See, J. Effective thermal conductivities of packed beds of chromite ores. *J. S. Afr. Inst. Min. Metall.* **1976**, *77*, 103–113.

53. Tang, C.; Yang, C.; Pan, J.; Zhu, D.; Lu, L.; Guo, Z. Oxidation Behavior of High FeO Ferrous Spinels and Its Impacts on the Induration Characteristics of Oxidized Pellets. *Metall. Mater. Trans. B* **2024**, *55*, 3072–3086. [CrossRef]
54. Kleynhans, E.; Beukes, J.; Van Zyl, P.; Fick, J. Techno-economic feasibility of a pre-oxidation process to enhance prereduction of chromite. *J. S. Afr. Inst. Min. Metall.* **2017**, *117*, 457–468. [CrossRef]